TOI-4641b: an aligned warm Jupiter orbiting a bright (*V*=7.5) rapidly rotating F-star

Allyson Bieryla [1,2]★ George Zhou,[2] Juliana García-Mejía,[1,3]† Tyler R. Fairnington,[1] David W. Latham,[1] Brad Carter,[2] Jiayin Dong,[4]‡ Chelsea X. Huang,[2] Simon J. Murphy,[2] Avi Shporer,[3] Karen A. Collins,[1] Samuel N. Quinn,[1] Mark E. Everett,[5] Lars A. Buchhave,[6] René Tronsgaard,[6] David Charbonneau,[1] Marshall C. Johnson,[7] Gilbert A. Esquerdo,[1] Michael Calkins,[1] Perry Berlind,[1] Jon M. Jenkins,[8] George R. Ricker,[3] Sara Seager,[3,9,10] Joshua N. Winn,[11] Thomas Barclay,[12] Ismael Mireles,[13] Martin Paegert[1] and Joseph D. Twicken[14]

[1]*Center for Astrophysics | Harvard & Smithsonian, 60 Garden Street, Cambridge, MA 02138, USA*
[2]*Centre for Astrophysics, University of Southern Queensland, West Street, Toowoomba, QLD 4350 Australia*
[3]*Department of Physics and Kavli Institute for Astrophysics and Space Research, Massachusetts Institute of Technology, Cambridge, MA 02139, USA*
[4]*Center for Computational Astrophysics, Flatiron Institute, 162 Fifth Avenue, New York, NY 10010, USA*
[5]*NSF's National Optical-Infrared Astronomy Research Laboratory, 950 N. Cherry Ave., Tucson, AZ 85719, USA*
[6]*DTU Space, Technical University of Denmark, Elektrovej 328, DK-2800 Kgs. Lyngby, Denmark*
[7]*Department of Astronomy, The Ohio State University, 4055 McPherson Laboratory, 140 West 18th Ave., Columbus, OH 43210 USA*
[8]*NASA Ames Research Center, Moffett Field, CA 94035, USA*
[9]*Department of Earth, Atmospheric and Planetary Sciences, Massachusetts Institute of Technology, 77 Massachusetts Ave, Cambridge, MA 02139, USA*
[10]*Department of Aeronautics and Astronautics, Massachusetts Institute of Technology, 77 Massachusetts Avenue, Cambridge, MA 02139, USA*
[11]*Department of Astrophysical Sciences, Princeton University, 4 Ivy Lane, Princeton, NJ 08544, USA*
[12]*NASA Goddard Space Flight Center, 8800 Greenbelt Road, Greenbelt, MD 20771, USA*
[13]*Department of Physics and Astronomy, University of New Mexico, 210 Yale Blvd NE, Albuquerque, NM 87106, USA*
[14]*SETI Institute, Mountain View, CA 94043, USA*

ABSTRACT

We report the discovery of TOI-4641b, a warm Jupiter transiting a rapidly rotating F-type star with a stellar effective temperature of 6560 K. The planet has a radius of 0.73 $R_{\rm Jup}$, a mass smaller than 3.87 $M_{\rm Jup}$ (3σ), and a period of 22.09 d. It is orbiting a bright star (*V*=7.5 mag) on a circular orbit with a radius and mass of 1.73 $R_\odot$ and 1.41 $M_\odot$. Follow-up ground-based photometry was obtained using the *Tierras* Observatory. Two transits were also observed with the Tillinghast Reflector Echelle Spectrograph, revealing the star to have a low projected spin-orbit angle ($\lambda=1.41^{+0.76°}_{-0.76}$). Such obliquity measurements for stars with warm Jupiters are relatively few, and may shed light on the formation of warm Jupiters. Among the known planets orbiting hot and rapidly rotating stars, TOI-4641b is one of the longest period planets to be thoroughly characterized. Unlike hot Jupiters around hot stars which are more often misaligned, the warm Jupiter TOI-4641b is found in a well-aligned orbit. Future exploration of this parameter space can add one more dimension to the star–planet orbital obliquity distribution that has been well sampled for hot Jupiters.

Key words: methods: observational – techniques: photometric – techniques: radial velocities – techniques: spectroscopic – exoplanets.

1 INTRODUCTION

Many hot Jupiters are thought to have formed at least a few astronomical units away from their stars and migrated inwards via dynamical interactions. One possible migration mechanism is high-eccentricity

★ E-mail: abieryla@cfa.harvard.edu
† 51 Pegasi b Fellow.
‡ Flatiron Research Fellow.

tidal migration, whereby their orbits gradually circularize with each periastron passage due to dissipative tidal interactions with their host stars (e.g. Rasio & Ford 1996). They may instead have formed *in situ* (e.g. Batygin 2012) or undergone disc-driven migration soon after their formation (e.g. Lin, Bodenheimer & Richardson 1996). Gas giants in somewhat longer period orbits, where tidal effects are negligible, provide useful laboratories for the study of the migration processes that produce hot Jupiters (Dawson & Johnson 2018).

Spin-orbit angle, the angle between the orbital normal and the spin-axis of the host star, serves as a fossil record of past dynamical

interactions experienced by the system. In particular, warm Jupiters, planets with $a/R_\star > 10$ and $R_p > 8\,R_e$, offer an opportunity to study the primordial obliquities of their host stars (Albrecht, Dawson & Winn 2022) without having to account for planet–star tidal interactions that may have modified the orbital architecture.

There exists clear trends in the hot Jupiter spin-orbit obliquity distribution as a function of stellar temperature (e.g. Albrecht et al. 2012). The dependence between the observed obliquity distribution and stellar temperature for longer period planets is less clear due to observational biases that make such observations more difficult. Close-in giant planets around cool stars ($T_{\mathrm{eff}} < 6250$ K) are generally observed to have well-aligned orbits (Albrecht, Dawson & Winn 2022). In contrast, more distantly orbiting giant planets about cool stars with $a/R_\star > 10$ show a wider range of spin-orbit angles, as in systems like WASP-8 (Queloz et al. 2010; Bourrier et al. 2017), Kepler-420 (Santerne et al. 2014), and HD 80 606 (Pont et al. 2009; Winn et al. 2009). Such a dependence is expected if the close-in planet obliquity distribution is strongly shaped by planet–star tidal interactions.

Short-period Jovian planets around early-type stars exhibit a wide distribution of orbital obliquities. Few long-period planets around hot stars have had their spin-orbit angles mapped. Kepler-448b is the only Jovian planet around an early-type star with an spin-orbit angle measured spectroscopically found to reside in a well-aligned orbit (Bourrier et al. 2015; Johnson et al. 2017).

The lack of well-characterized long-period planets around early-type stars prohibits informative tests on the mechanisms thought to induce misalignments in planet orbits. Early-type stars with radiative envelopes experience weaker planet–star tidal interactions and offer the opportunity of exploring the primordial period obliquity relationship for giant planets. Each mechanism that induces planet–star misalignments have their own expected dependencies on orbital distance. Warps in the protoplanet disc lead to preferentially longer period planets being found in misaligned orbits (Heller 1993; Wijnen et al. 2017). The spin-axis of stars hotter than the Kraft break (Kraft 1967) may also evolve over time by itself. Gravity-wave instabilities induced at the radiative–convective boundary of early-type stars may result in their outer envelopes changing in spin-axis over time (Rogers, Lin & Lau 2012), leading to a wide range of spin-orbit obliquites for planets around such stars. Such instabilities are not dependent on the planetary system, and as such no period-spin-orbit obliquity dependencies should be expected.

In this paper we report the planetary confirmation of TOI-4641b, a warm Jupiter on a 22-d orbit that is well aligned with the equatorial plane of a rapidly rotating F-star. In Section 2, we describe the photometric data from *TESS* and the *Tierras* Observatory, high-resolution speckle imaging, and Tillinghast Reflector Echelle Spectrograph (TRES) spectroscopic observations to measure the stellar obliquity. Section 3 describes the global modelling of the system and Section 4 describes the stellar variability. We conclude with a discussion in Section 5.

2 OBSERVATIONS

2.1 Photometric observations

2.1.1 TESS photometry

The *Transiting Exoplanet Survey Satellite* (*TESS*; Ricker et al. 2015) is an all-sky survey searching for transiting exoplanets around nearby bright host stars. The satellite uses four cameras to stare at 24×96 deg sectors of the sky for approximately 27 d at a time. TOI-4641 (TIC 436873727) was observed by *TESS* during Sector 18 of the primary mission and then again in Sectors 42, 43, 44, and 58 of the extended mission, in all cases with 2-min cadence. The data were processed by the NASA Science Processing Operations Center pipeline (SPOC; Jenkins et al. 2016) and the light curves were downloaded from the Mikulski Archive for Space Telescopes (MAST)[1] using the *Lightkurve* package (Lightkurve Collaboration 2018). The Presearch Data Conditioning Simple Aperture Photometry [PDCSAP; (Smith et al. 2012; Stumpe et al. 2012, 2014)]] light curves were employed in our analysis and are plotted in Fig. 1. Sector 44 was excluded from our planet analysis because the transit occurred at the edge of a gap in the light curve.

A candidate exoplanet orbiting TOI-4641 with a period of 22.1d was identified in light curves including data through Sector 43 in both SPOC (Jenkins et al. 2016) and QLP (Huang et al. 2020; Kunimoto et al. 2022) pipelines. The SPOC performed a transit search with an adaptive, noise-compensating matched filter (Jenkins 2002; Jenkins et al. 2010, 2020), producing a Threshold Crossing Event (TCE) for which an initial limb-darkened transit model was fitted (Li et al. 2019) and a suite of diagnostic tests were conducted to help assess the planetary nature of the signal (Twicken et al. 2018). The QLP performed its transit search with the Box Least Squares Algorithm (Kovács, Zucker & Mazeh 2002). The transit signature passed all SPOC data validation diagnostic tests, and the TESS Science Office issued an alert (Guerrero et al. 2021) for TOI 4641.01 on 2021 November 19. The difference image centroid offsets localized the transit source for TOI 4641.01 within 2.4 ± 2.5 arcsec; all TIC v8 (Stassun et al. 2019) objects other than TOI-4641 were excluded as potential sources of the transit signature.

2.1.2 Ground-based photometry

To check the field for nearby eclipsing binaries that could potentially be contaminating the *TESS* photometry and to confirm the transit was on the target star, we used the TESS TRANSIT FINDER, a customized version of the TAPIR software package (Jensen 2013), to schedule ground-based transit observations. Follow-up observations were done using the *Tierras* Observatory (Garcia-Mejia et al. 2020) at the Fred Lawrence Whipple Observatory atop Mount Hopkins in AZ, USA. *Tierras* is a 1.3m telescope with a Teledyne e2v 4K $\times$ 4K NIR-optimized deep-depletion CCD. It has a 0.48×0.25 deg field of view and a 0.43 arcsec per pixel scale. The camera was designed to have a custom narrow (40 nm full width at half-maximum) bandpass filter centred around 863.5 nm to minimize precipitable water vapor errors known to limit ground-based photometry of M dwarfs.

The data were reduced using a custom pipeline based on similar procedures as outlined in Irwin et al. (2015) and aperture photometry was performed using ASTROIMAGEJ (AIJ, Collins et al. 2017). Two partial transits were observed on UT 2022 December 17 (egress) and UT 2023 January 30 (ingress). A full transit was observed on UT 2023 January 8. The transits on the nights UT 2022 December 17 and UT 2023 January 8 coincided with the spectroscopic observations described in more detail in Section 2.2.1. We extracted the photometry using an aperture radius of 12 pixels (5.16 arcsec) from the data on UT 2022 December 17 to determine that the target star was the source of the transit events and we excluded any star more distant than 5 arsec as the source of the dips observed by *TESS*. That light curve is shown in Fig. 2 along with the phase-folded *TESS* light curve. We note $\sim$6 h variation in the ground-based light curve at
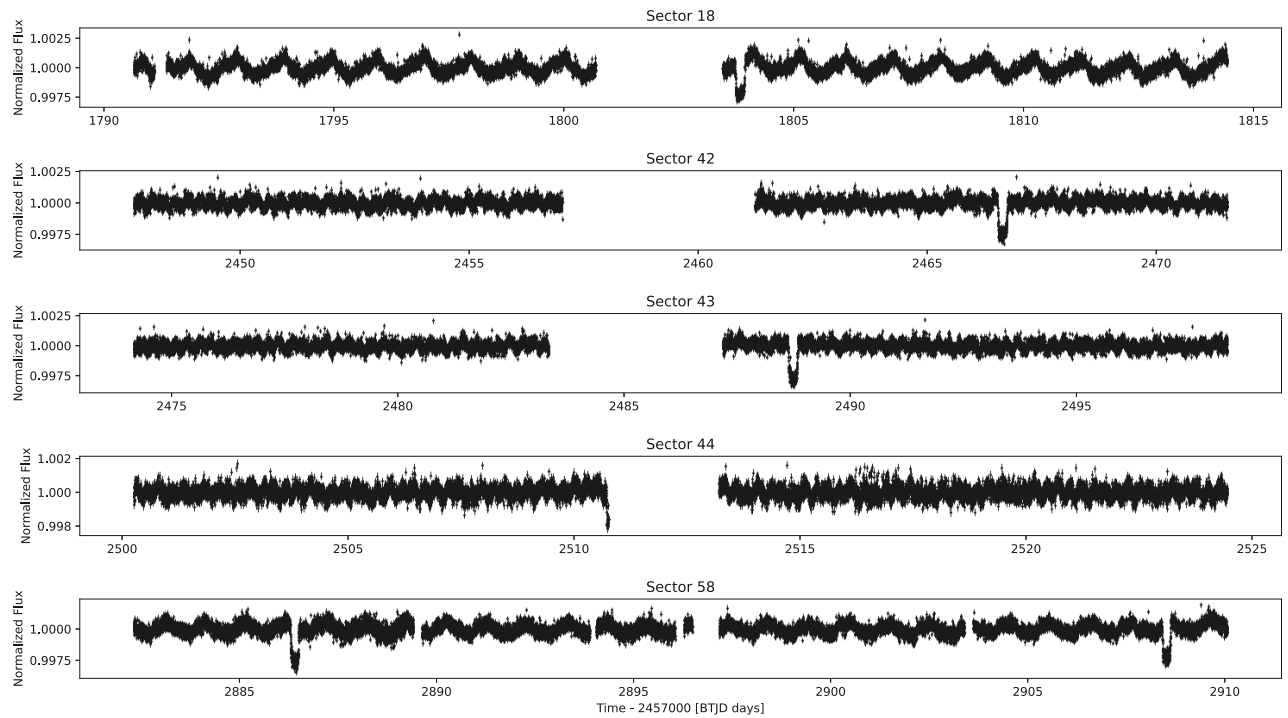
Figure 1. Per-sector Normalized TESS PDCSAP light curves for TOI-4641. The target star was observed over five TESS sectors. Because the Sector-44 data set covers only one part of one transit, this data set was not included in our global modelling of the planetary properties. Significant stellar variability is seen within each sector of the TESS observations, as discussed in Section 4.
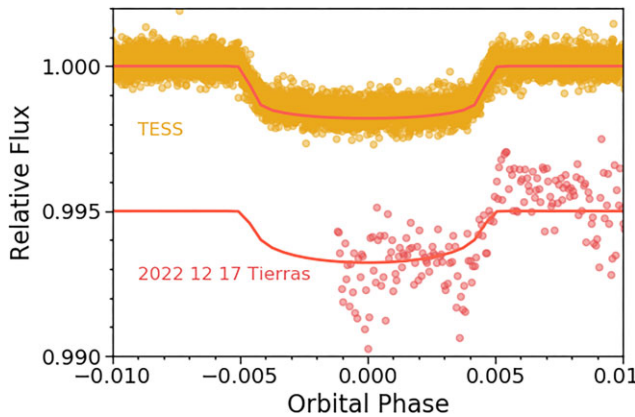

Figure 2. *Top:* Phase-folded *TESS* light curves of five transits from Sectors 18, 42, 43, and 58. The best-fitting model from the global modelling analysis is illustrated as a red line. *Bottom:* Follow-up observations from the *Tierras* Observatory, capturing the egress event on UT 2022 December 17.

the ∼1 mmag level. The light-curve variability is discussed in more detail in Section 4. Data from the nights of UT 2023 January 8 and 30 were not of sufficient quality to add any value to the fit due to poor observing conditions and experimental exposure times leading to occasional saturation and were not included in the global analysis. The photometric analysis files from AIJ are all available publicly on the Exoplanet Follow-up Observing Program (ExoFOP)[2] website.

2.1.3 High-resolution imaging

We observed TOI-4641 on UT 2023 February 5 using NESSI (Scott et al. 2018), a speckle imager at the WIYN 3.5m telescope. The observations consisted of taking speckle sequence data in two filters with central wavelengths of 562 and 832 nm. We reduced these data using the standard speckle pipeline (Howell et al. 2011) to obtain reconstructed images of the focal plane as well as a contrast curve centred on the target star and extending out to a radius of 1.2 arcsec. No secondary sources were detected surrounding TOI-4641. The background limit plots are shown in Fig. 3.

2.2 Spectroscopic observations

2.2.1 Radial velocity observations

A single observation of TOI-4641 was obtained on UT 2021 November 23 with the NRES (Siverd et al. 2018) spectrograph located at the Las Cumbres Observatory (Brown et al. 2013) node at McDonald Observatory, TX, USA. Two successive 900 s observations were stacked and reduced via the BANZAI-NRES pipeline (McCully et al. 2022) to estimate a $v\sin I_\star$ of approximately 90 km s^{-1}, indicating that TOI-4641b was a favourable target for further investigation into the projected spin-orbit angle.

Spectroscopic observations were obtained with the TRES (Fűrész 2008) as part of the TESS Follow-up Observing Program SubGroup 2 Reconnaissance Spectroscopy program. TRES is an optical (3900–9100 Å) fibre-fed echelle spectrograph on the 1.5m Tillinghast Reflector at the Fred Lawrence Whipple Observatory (FLWO) in AZ, USA. The spectrograph has a resolving power of $R \sim 44\,000$.

TOI-4641 was first observed on UT 2021 November 30 with an exposure time of 180 s leading to a signal-to-noise per resolution
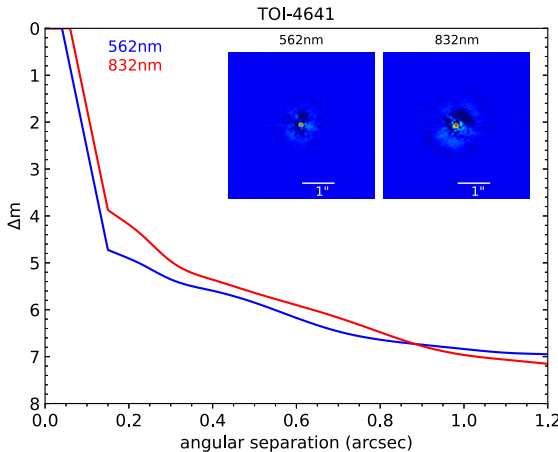
Figure 3. Contrast curves based on NESSI speckle imaging of TOI-4641 in two filters centred at 562 nm (blue curve) and 832 nm (red curve). Speckle imaging analysis was confined to the inner 1.2 arcsec of the full 4.6 × 4.6 arcsec field of view. Speckle reconstructed images centred on the star are inset at the top of the figure. We find no companions to TOI-4641 in these high-resolution imaging observations.

element (SNRe) of 113. The quick-look classification showed that the host star was rapidly rotating. Despite the rapid rotation which would make precise radial velocities very challenging, a second TRES spectrum (SNRe of 131) at opposite orbital quadrature was obtained on UT 2021 December 21 to check for a large velocity variation that would be indicative of a stellar companion. The velocity offset between the two spectra was ∼275 m s^{-1} based on the standard TRES pipeline which derives velocities using a single order of the spectrum centred on the Mg b features as described in Buchhave et al. (2010). An additional 13 TRES observations were obtained between UT 2022 December 10 and 31 with longer exposures than the original reconnaissance spectra in an attempt to gain high enough SNRe to detect an orbital solution. The average SNRe of the new observations was 195.

In an attempt to get the best velocity precision, we used a least squares deconvolution technique (Zhou et al. 2016) based on the methods of Donati et al. (1997) and Collier Cameron et al. (2010) to extract radial velocities. Due to the rapid rotation of the host star, we were unable to detect an orbital signal of the planet. We also tried a multispectral order analysis of the available spectra. Each spectrum was cross-correlated order-by-order against the highest SNRe observed spectrum to derive relative multi-order velocities. While we again were unable to detect a clear orbital signal, we were able to determine a 3σ upper limit planetary mass of 3.87 M_{Jup}. The least squares deconvolution velocities are presented in Table 1, and were adopted for further analysis in Section 3. In addition, we also modelled the line profile determined from each spectrum to derive rotational and macroturbulent broadening velocities for the host star. The line profile is modelled as per Gray & Corbally (1994), with the macroturbulent broadening component described via a radial-tangential model. We find the best-fitting rotational broadening velocity of 86.3 ± 1.0 km s^{-1}, and a macroturbulent velocity of 4.00$^{+0.62}_{-0.66}$ km s^{-1} for TOI-4641.

2.2.2 Transit spectroscopic observation

As a planet transits across its host star's stellar disc, a portion of the stellar blue- and red-shifted light is blocked, which produces a shift in the radial velocity measurements. This effect, known as the

Table 1. TRES recon radial velocities.

Time (BJD$_{TDB}$)	Velocity (km s^{-1})	Uncertainty (km s^{-1})
2459548.73116	24.12	0.26
2459560.66830	24.35	0.22
2459923.66941	24.34	0.29
2459924.68547	24.58	0.31
2459925.70482	24.53	0.21
2459928.73172	24.31	0.27
2459929.73860	24.19	0.32
2459933.80715	24.56	0.31
2459934.80076	24.49	0.28
2459935.67590	24.58	0.30
2459936.82834	24.53	0.22
2459937.70062	24.44	0.27
2459938.74970	24.52	0.30
2459939.81605	24.51	0.26
2459944.75598	24.34	0.30

Rossiter–McLaughlin (Rossiter 1924 and McLaughlin 1924) effect, allows us to measure the projected spin-orbit angle of a transiting system.

To determine the projected spin-orbit angle, spectra were obtained during two transits on UT 2022 December 17 and UT 2023 January 8 using the TRES spectrograph. Spectra were acquired in the standard way by obtaining a set of three 300 s exposures surrounded on either side by Thorium–Argon calibration spectra. The three spectra were then combined using cosmic ray rejection and run through the standard TRES pipeline as described in Section 2.2.1. We observed a partial ingress on the night of UT 2022 December 17 collecting 18 sets of three spectra and a full transit on UT 2023 January 8 of 39 sets of three spectra with an average SNRe of 147 and 195, respectively.

To extract the planetary Doppler shadow, we derived the line-broadening profiles for each observation in an analysis similar to that described above. We performed a least squares deconvolution between the observed spectra and a synthetic ATLAS9 stellar template (Castelli & Kurucz 2004), generated at the atmospheric parameters of the host star, with no rotational broadening incorporated. We then modelled the differences between each derived line profile and the median combined line profile measured over the transit night as part of our global modelling analysis as per Zhou et al. (2019). Briefly, for each observation, we calculated the integrated line profile of the portion of the star blocked by the planet. This incorporates the effects of local limb darkening, macroturbulent broadening, and rotation. This is modelled simultaneously with the system parameters as part of the global modelling process (Section 3). The line profile residuals for each transit observation, and for the combined observations, are shown in Fig. 4. The dark trail from bottom left to top right represents the shadow of the planet during the transit in the line profile residuals.

2.2.3 Stellar parameters from TRES spectra

We used the Stellar Parameter Classification (SPC; Buchhave et al. 2012) tool to derive stellar parameters using the TRES spectra. SPC cross-correlates an observed spectrum against a library grid of synthetic spectra calculated using the Kurucz (1992) atmospheric models. A ∼310 Å region of the spectrum surrounding the Mg b lines is used to derive effective temperature, T_{eff}, surface gravity, log g, rotational velocity, $v \sin i$, and metallicity, [m/H]. Metallicity is derived using all available metal lines rather than just the Fe lines and therefore reported as [m/H] but is closely related to [Fe/H] values.
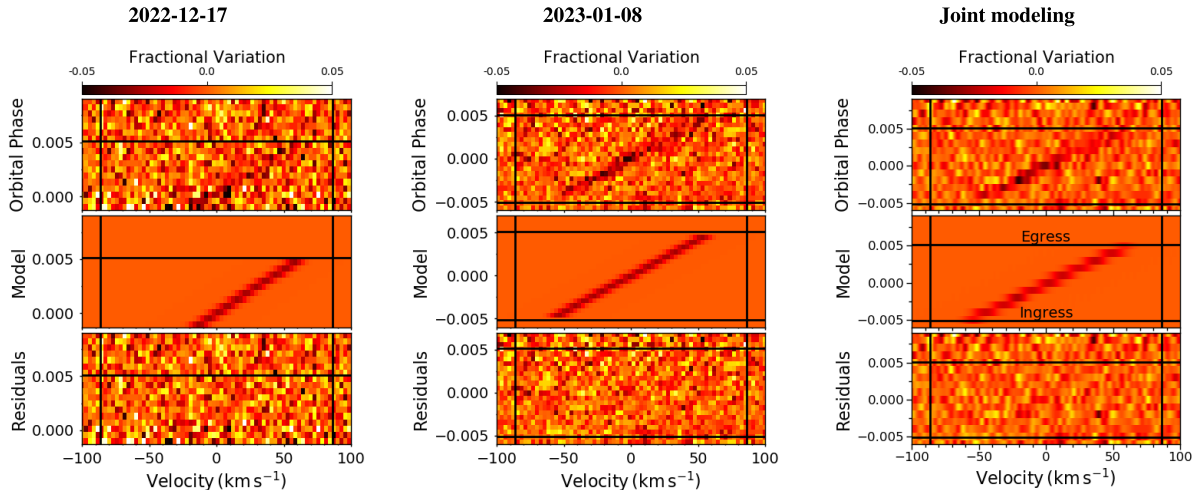
Figure 4. TRES Doppler spectroscopic results. The colour scale represents the fractional variation in the spectral line profile. Each plot shows the planetary signal after the average rotational profile is subtracted (top), the best-fitting model (middle), and the residuals after subtracting the planetary signal (bottom). Left: Doppler spectroscopy egress transit event on 2022 December 17. Middle: Doppler spectroscopy observations from the full transit event on 2023 January 8. Right: the combined Doppler spectroscopy result from the two TRES transit observations. The vertical lines are the $v\sin i$ boundaries, while the horizontal lines mark the ingress and egress timings.
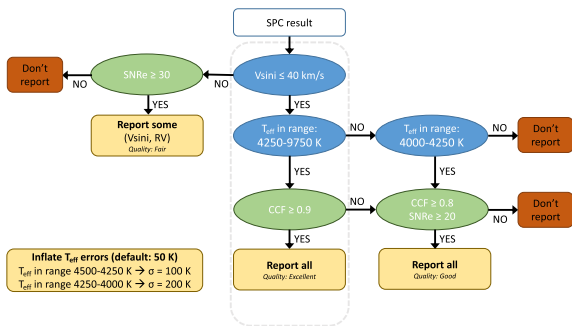
Figure 5. SPC QF decision tree assigns a QF – Excellent, Good, Fair, and Poor – based on the known limitations of SPC. The QF reliability of the result uses the stellar effective temperature, rotational velocity, SNRe, and the CCF peak value as quality indicators.

We recently developed a quality flag (QF) metric – Excellent, Good, Fair, and Poor – for SPC results based on the known limitations of SPC. Each spectrum is run through an algorithm (shown in Fig. 5) to determine the reliability of the result using stellar effective temperature, rotational velocity, SNRe, and the cross-correlation function (CCF) peak value as quality indicators. As a service to the community, SPC stellar parameters for all TRES spectra of *TESS* targets are uploaded to the ExoFOP website when the QF is Excellent or Good. If the QF is determined to be Fair, as in the case of TOI-4641 due to the high stellar rotational velocity, the stellar parameters are not considered reliable and only the rotational velocity of the star is uploaded. Stellar parameters are not uploaded when a QF of Poor is determined.

SPC reports a $v\sin i$ of 91.60 ± 0.50 km s^{-1} for TOI-4641 but because SPC does not solve for macroturbulence and the Least Squares Deconvolution analysis does, we chose to use the Least Squares Deconvolution reported value as determined in Section 2.2.1 (86.3 ± 1.0 km s^{-1}) as a prior for our global analysis. The SPC uncertainty reported is the floor error and should be inflated due to the star's rapid rotation.

2.3 SED analysis

We used all available broad-band photometry, including *Hipparcos B* and *V* bands (Perryman et al. 1997), *Gaia* DR3 *G*, *Bp*, *Rp* (Gaia Collaboration 2023), 2MASS *J*, *H*, *K* (Skrutskie et al. 2006), and WISE W_1, W_2, W_3, W_4 bands (Cutri et al.), as well as *Gaia* DR3 parallaxes to model the spectral energy distribution of TOI-4641. The spectral energy distribution is modelled simultaneously with the photometric and spectroscopic observations of the system, such that the stellar properties derived are jointly constrained by the transit and the photometric properties of the star. At each iteration of the global model (Section 3), we compute the interpolated isochrone magnitudes for each tested stellar mass, age, and metallicity. We then compute the log likelihood between the isochrone magnitudes and the observed values and associated uncertainties for each band. We adopt the MIST isochrones (Dotter 2016), interpolated via the MINIMINT package (Koposov 2020), for our stellar models. The best-fitting model, as per Table 2, is shown in Fig. 6.

3 GLOBAL MODELLING

To determine the stellar and planetary parameters of the system holistically, we performed a joint analysis of all available photometric, spectroscopic, and catalogue observations. This included photometric transit observations from TESS and *Tierras* (Sections 2.1.1 and 2.1.2), two spectroscopic transit observations from TRES (Section 2.2.2), the TRES out-of-transit radial velocities (Section 2.2.1), and available catalogue observations (Section 2.3). Free parameters largely describing the transit include the orbital period P, reference time of transit centre T_0, planet-to-star radius ratio $R_p/R_\star$, line-of-sight inclination i, and orbital eccentricity parameters $\sqrt{e}\cos\omega$ and $\sqrt{e}\sin\omega$. In addition, the radial velocity orbit is modelled by including the free parameter describing the mass of the planetary companion M_p. The spectroscopic transit is modelled as per Zhou et al. (2019), with free parameters including the projected spin-orbit angle λ, rotational broadening $v\sin I_\star$, and macroturbulent broadening velocity. Simultaneous with the transit models, we also interpolate the stellar isochrones as per Section 2.3. At each step, we model the spectral energy distribution to constrain the stellar

Table 2. Stellar parameters for TOI-4641.

Stellar parameters	Value	Source
Catalogue information		
TIC ID	436 873 727	TESS TOI Catalog
TOI ID	4641	TESS TOI Catalog
Gaia DR3 ID	114 340 658 009 875 072	GAIA DR3
2MASS ID	J02501388+2520010	2MASS
TYC ID	1785-00801-1	Tycho
Coordinates and proper motion		
Right ascension (h:m:s)	02:50:13.90 (J2000)	GAIA DR3
Declination (d:m:s)	25:20:01.00 (J2000)	GAIA DR3
Parallax (mas)	11.409 ± 0.026	GAIA DR3
$\mu_{R.A}$ (mas yr^{-1})	61.447 ± 0.027	GAIA DR3
$\mu_{Dec.}$ (mas yr^{-1})	-20.020 ± 0.024	GAIA DR3
Magnitudes		
TESS (mag)	7.1323 ± 0.0061	TESS TOI Catalog
G (mag)	7.42334 ± 0.00031	GAIA DR3
B_p (mag)	7.60660 ± 0.00093	GAIA DR3
R_p (mag)	7.09227 ± 0.00057	GAIA DR3
B (mag)	7.895 ± 0.027	Tycho
V (mag)	7.51 ± 0.030	Tycho
J (mag)	6.746 ± 0.020	2MASS
H (mag)	6.639 ± 0.023	2MASS
K (mag)	6.579 ± 0.029	2MASS
$WISE_{3.4\mu}$ (mag)	6.552 ± 0.081	WISE
$WISE_{4.6\mu}$ (mag)	6.527 ± 0.024	WISE
$WISE_{12\mu}$ (mag)	6.588 ± 0.016	WISE
$WISE_{22\mu}$ (mag)	6.426 ± 0.085	WISE

Note. TESS TOI Primary Mission Catalog; (Guerrero et al. 2021), Tycho; (Høg et al. 2000); GAIA DR3; (Gaia Collaboration 2023), 2MASS; (Cutri et al. 2003), WISE; (Cutri et al. 2021a).
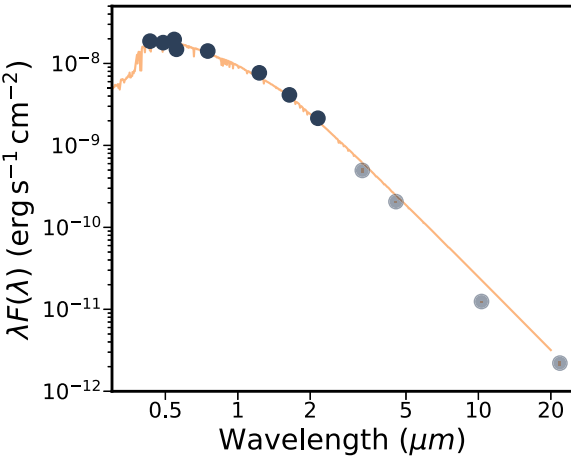

Figure 6. Spectral energy distribution of the target star TOI-4641. Magnitudes from *Gaia G*, B_p, R_p, *Tycho B*, *V*, 2MASS *J*, *H*, *Ks* are included in the global modelling of the system and are shown in dark blue. Magnitudes from WISE *W1*, *W2*, *W3*, and *W4* are shown in light grey but not included in the model.

parameters. Free parameters describing the stellar isochrone and spectral energy distribution modelling include stellar mass $M_\star$, age, metallicity [m/H], and parallax.

A number of parameters are constrained by informed priors in the global modelling. Parallax is tightly constrained by a Gaussian prior about its *Gaia* DR3 value and associated uncertainties. Rotational and macroturbulent broadening velocities are constrained by Gaussian priors about their spectroscopically determined values. Stellar metal-

licity is constrained by a Gaussian prior about the SPC-determined value. Uniform priors about reasonable physical parameter spaces are adopted for all other free parameters. The adopted priors are noted in Table 3. Gaussian priors are noted as $\mathcal{G}(\mu, \sigma)$, while uniform priors and their adopted ranges are noted by $\mathcal{U}(\text{min}, \text{max})$.

The photometric transits are modelled as per Mandel & Agol (2002) via the BATMAN package (Kreidberg 2015). Limb darkening parameters are interpolated and fixed to their values as per Claret & Bloemen (2011), Claret (2017), and Eastman, Gaudi & Agol (2013). The spectroscopic transit is modelled as per Section 2.2.2, via a disc integration of the portion of the stellar surface occulted by the planet, incorporating the effect of local macroturbulence and rotational broadening.

The best-fitting parameters are presented in Tables 2 and 3. A number of additional parameters are derived from the posterior chains and reported in Table 3 for completeness. These are marked as 'inferred' in the table. Stellar parameters for luminosity, effective temperature, surface gravity, and age are rederived from MIST isochrones interpolations for each given link in the MCMC chain subsequent to the global modelling. Planet properties, including radius, orbital semimajor axis, eccentricity, and transit impact parameter are subsequently derived from the posteriors. In addition to the global model, we also propagate the posteriors and follow Masuda & Winn (2020) to derive the 3D spin-orbit obliquity of the system. We use the rotational period (see Section 4), line broadening, and projected spin-orbit angle to derive a 3D orbital obliquity of $2.4 \pm 1.3°$.

4 STELLAR VARIABILITY

TOI-4641 exhibits short time-scale stellar variability at the 1 mmag level during all five sectors of *TESS* observations and is also noticed in the ground-based observations. The variability is likely consistent with changing rotational spot modulation on the stellar surface.

The top left panel of Fig. 7 shows the sector-by-sector frequency power spectrum of TOI-4641. Sectors 18 and 58 exhibit variability at the 0.96 ± 0.02 cycles d^{-1} frequency, while the 3.93 ± 0.02 cycles d^{-1} peak is strongest for Sectors 42, 43, and 44. The variability does not exhibit equal period spacing as is expected for γ Dor variables, and the frequency is too low for δ Scuti pulsations. We suggest the variability is most consistent with rotational modulation. The rotational broadening velocity $v \sin I_\star = 86.3 \pm 1.0$ km s^{-1} propagates to an expected rotation period of 1.06 ± 0.04 d assuming $\sin I_\star = 1$, corresponding to 0.94 ± 0.04 cycles d^{-1}, which is consistent with the peak variability frequency in the light curve in Sectors 18 and 58. The 1 cycle d^{-1} periodicity is the second most dominant peak in Sectors 42, 43, and 44, with the 4 cycles d^{-1} peak likely due to the specific spot configuration during this timeframe. Low-amplitude spot variability is seen in early-type stars in the *Kepler* sample. Sikora, Wade & Rowe (2020) note that 10–30 per cent of A and B stars exhibit spot-induced variability, despite not showing spectroscopic signatures of chemical peculiarity. Using all *TESS* sectors of data, we derive a 3σ lower limit on the stellar inclination $I_\star$ of $83°$.

To check if the variability is on target, we used the LIGHTKURVE code (Lightkurve Collaboration 2018) to extract light curves from multiple target and background apertures, and found no changes in the amplitude and shape of the variability. Fig. 8 shows a set of example target apertures and resulting light curves. The target is in a sparse field and there are no stars within a 1 arcmin field that are bright enough to cause the 1 mmag variability seen on target after dilution. We also note that the rotational modulation was similarly identified in the SPOC transit search of the combined TOI-4641 light curves.

Table 3. Best-fitting stellar and planetary properties for TOI-4641.

Parameters	Description (Units)	Prior values	Best fit
Stellar parameters:			
$M_\star$	Stellar mass ($M_\odot$)	$\mathcal{U}(1.2, 3.5)$	$1.41^{+0.068}_{-0.059}$
$R_\star$	Stellar radius ($R_\odot$)	$\mathcal{U}(1.2, 3.5)$	$1.72^{+0.041}_{-0.043}$
$L_\star$	Stellar luminosity ($L_\odot$)	Inferred	$4.95^{+0.94}_{-1.21}$
$T_{\rm eff}$	Effective temperature (K)	Inferred	6560^{+300}_{-340}
$\log g$	Surface gravity (cgs)	Inferred	$4.11^{+0.69}_{-0.69}$
[m/H]	Metallicity (dex)	$\mathcal{G}(-0.2, 0.2)$	$-0.09^{+0.11}_{-0.18}$
$v\sin I_\star$	Projected rotational velocity ($\rm km\,s^{-1}$)	$\mathcal{G}(86.3, 1.0)$	$86.3^{+1.00}_{-0.99}$
$v_{\rm macro}$	Macroturbulent velocity ($\rm km\,s^{-1}$)	$\mathcal{G}(5.5, 7.7)$	$4.00^{+0.62}_{-0.66}$
Parallax	Parallax (mas)	$\mathcal{G}(11.409, 0.026)$	11.409 ± 0.025
Age	Age (Gyr)	Inferred	$2.69^{+0.81}_{-1.14}$
Distance	Distance (pc)	Inferred	$87.60^{+0.20}_{-0.20}$
$I_\star$	Stellar Inclination (deg)	Derived	$>83\,(3\sigma)$
$u_{1,\rm TESS}$	Limb darkening coefficient	Fixed	0.197
$u_{2,\rm TESS}$	Limb darkening coefficient	Fixed	0.317
$u_{1,\rm Tierras}$	Limb darkening coefficient	Fixed	0.209
$u_{2,\rm Tierras}$	Limb darkening coefficient	Fixed	0.314
Planetary parameters:			
P	Orbital period (d)	$\mathcal{U}(22.09, 22.10)$	$22.093410^{+0.000051}_{-0.000047}$
T_o	Epoch (BJD)	$\mathcal{U}(245910.80, 245910.85)$	$2459510.82759^{+0.00091}_{-0.00100}$
M_p	Planet mass ($M_{\rm Jup}$)	$\mathcal{U}(0, 105)$	$<3.87\,(3\sigma)$
R_p	Planet radius ($R_{\rm Jup}$)	Inferred	$0.730^{+0.026}_{-0.028}$
$R_p/R_\star$	Radius of planet to star ratio	$\mathcal{U}(0.01, 0.1)$	$0.042^{+0.0009}_{-0.0009}$
$a/R_\star$	Semimajor axis to star radius ratio	Inferred	$21.53^{+0.51}_{-0.52}$
a	Semimajor axis (au)	Inferred	$0.173^{+0.015}_{-0.015}$
e	Eccentricity	Inferred	$<0.074\,(3\sigma)$
$\sqrt{e}\cos\omega$	Eccentricity parameter	$\mathcal{U}(-0.2, 0.2)$	$0.01^{+0.13}_{-0.14}$
$\sqrt{e}\sin\omega$	Eccentricity parameter	$\mathcal{U}(-0.2, 0.2)$	$0.03^{+0.12}_{-0.13}$
γ	Radial velocity offset ($\rm km\,s^{-1}$)	$\mathcal{U}(24, 25)$	$24.400^{+0.077}_{-0.072}$
T_{14}	Transit duration (d)	Inferred	$0.2266^{+0.0029}_{-0.0030}$
i	Orbital inclination (deg)	$\mathcal{U}(80, 110)$	$87.90^{+0.088}_{-0.084}$
b	Impact parameter	Inferred	$0.780^{+0.014}_{-0.015}$
λ	Projected spin-orbit angle (deg)	$\mathcal{U}(-185, 185)$	$1.41^{+0.76}_{-0.76}$
ψ	3D orbital obliquity (deg)	Derived	2.4 ± 1.3

Note. Gaussian priors are listed as $\mathcal{G}$(median,width) and uniform priors are listed as $\mathcal{U}$(lower bound, upper bound). Inferred parameters are calculated from the posterior distribution. TRES spectra were used to derive a metallicity prior using the SPC analysis (Buchhave et al. 2012) and the project rotational velocity and macroturbulent velocity using a least squares deconvolution analysis (Zhou et al. 2016). Parallax was obtained from the *Gaia* DR3 release (Gaia Collaboration 2023).

These TCEs attributed to the rotational modulation were subjected to the same diagnostic tests as would any TCE triggered by a transiting planet. The difference image centroid offsets (Twicken et al. 2018) showed that the source of the modulation was consistent with TOI-4641 at the 3σ level and inconsistent at that level with all other TIC v8.2 objects.

5 DISCUSSION

TOI-4641 is a warm Jupiter in a 22 d orbit around a bright (V=7.5), rapidly rotating ($86.3^{+1.00}_{-0.99}\,\rm km\,s^{-1}$) F-star. The orbit is nearly circular with eccentricity constrained at the 3σ level to less than 0.074. This target was observed in five *TESS* sectors and was photometrically followed up by the *Tierras* ground-based Observatory to rule out the false positive scenario of a nearby eclipsing binary contaminating

the aperture. Additionally, we obtained high-resolution images from the Speckle imager on the WIYN 3.5m telescope and detected no secondary sources out to a radius of 1.2 arcsec. TRES spectra allowed us to detect a 3σ upper limit planetary mass of 3.87 $M_{\rm Jup}$. We also obtained two nights of TRES in-transit spectroscopic data to measure the projected spin-orbit angle of $1.41^{+0.76\circ}_{-0.76}$.

TOI-4641b is amongst the longest period planets to be thoroughly characterized about a hot rapidly rotating star (Fig. 9). Long-period planets provide tests for mechanisms that induce primordial misalignment in planetary systems. At such orbital distances, star–planet tidal interactions are too weak to modify the orbital obliquity.

Chaotic accretion is one proposed method of primordial misalignments where neighbouring protostar material interacts or arrives at different times during the accretion process, potentially causing the protostar disc to tilt with respect to the star (Bate, Lodato & Pringle
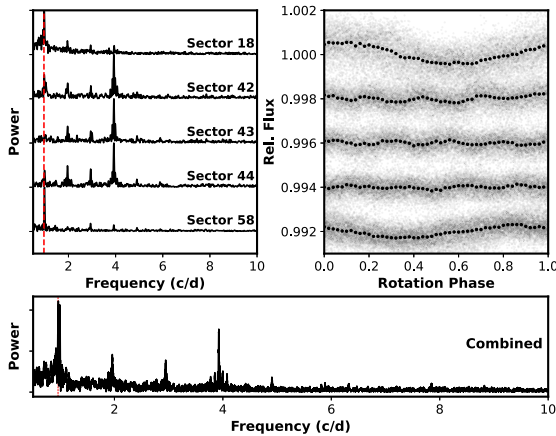
Figure 7. TOI-4641 exhibits 1 d time scale variability over all observed *TESS* sectors. The per sector frequency spectra are shown in the *top left* panel. The frequency spectrum of the entire *TESS* data set is shown on the *bottom*. The per sector light curves, folded to the 0.96 cycles d^{-1} frequency, are shown on the *top right* panel. The 0.96 cycle per day peak is consistent with the expected rotation period of the star as per the spectroscopic rotational line broadening velocity. We interpret the variability to be spot-induced modulations, with the spots likely changing in configuration over multiple months.
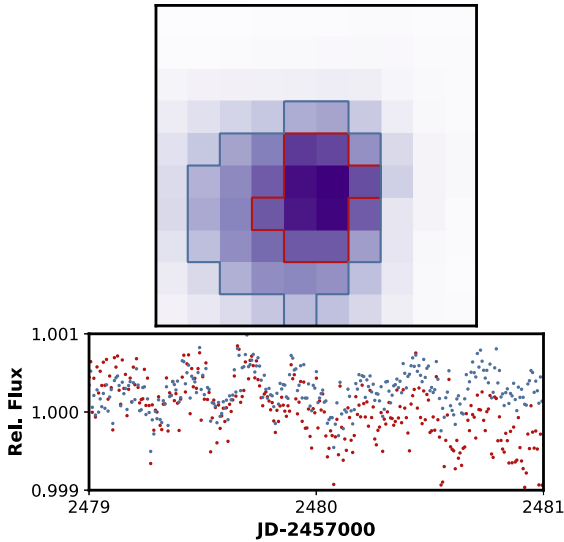
Figure 8. Photometry, using two different apertures, showing that the observed variability is likely on target and not induced by a nearby background source. The *top* panel shows a narrow 90-percentile (red) and a broad 50-percentile (blue) aperture. The *bottom* panel shows a 2-d example section of their respective light curves showing no difference in the frequency and amplitude of the observed light curve as a function of aperture size.

2010; Thies et al. 2011; Fielding et al. 2015; Bate 2018; Kuffmeier et al. 2021). Another proposed mechanism for misalignment is magnetic warping. In young stars, in particular, the twisting of magnetic field lines between the ionized disc and the differential rotation of the young star can cause misalignment (Foucart & Lai 2011; Lai 2012). In this scenario, the misalignment torque must overcome the realignment torque from accretion, magnetic braking, disc winds, and viscosity. Stellar or planetary companions can also cause misalignment during the primordial phase of formation (Borderies, Goldreich & Tremaine 1984; Lubow & Ogilvie 2000; Batygin 2012; Matsakos & König 2017). Rogers, Lin & Lau (2012) proposed that
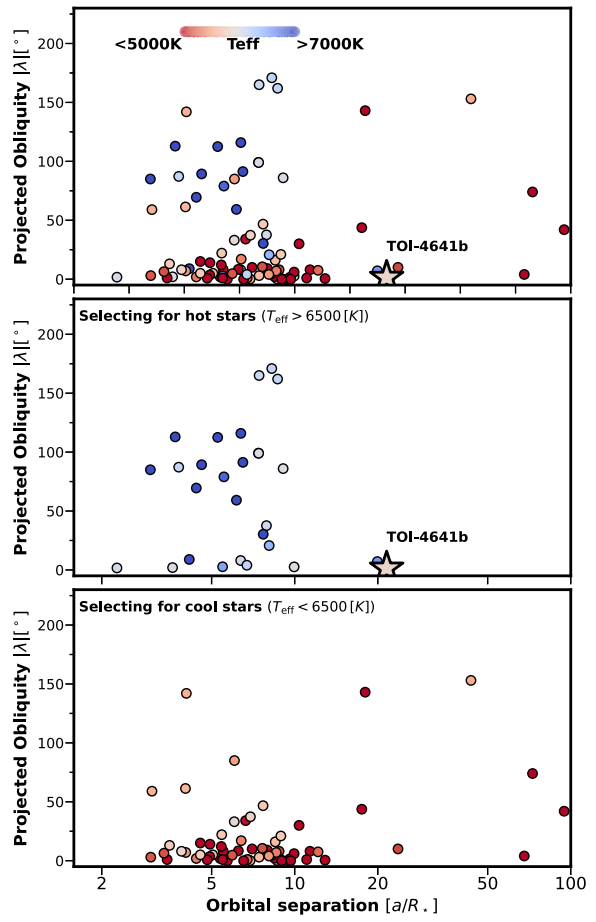
Figure 9. TOI-4641b amongst giant planets with obliquities measured. Top: obliquity as a function of $a/R_\star$; values are adopted from Albrecht, Dawson & Winn (2022) including only planets with $R_p > 8\,R_e$ to represent the Jovian population. The colours represent the effective temperature of the host star. TOI-4641b is represented with a star. Middle: selecting only for planets about stars $T_{\rm eff} > 6500\,K$. TOI-4641 is one of the longest period planets characterized about an early-type star. Bottom: the distribution for planets about cool stars $T_{\rm eff} < 6500\,K$.

internal gravity waves excited at the radiative–convective boundary of early-type stars can induce their surface layers to change in spin direction. Changes to the spin axes of early-type stars will also lead to an apparent spin-orbit misalignment, potentially contributing to the temperature-obliquity gradient seen in the hot Jupiter population.

Critically, most of these proposed mechanisms do not have a strong dependence on the host star properties beyond planet–star tidal interactions. We should not observe strong differences in the obliquity distributions of longer period Jovian planets as a function of stellar mass. Should internal gravity waves (Rogers, Lin & Lau 2012) play a major role in shaping the spin axes of early-type stars, no orbital distance trends should be observed in that population.

Testing these predictions motivate full characterizations of planets in long-period orbits about early-type stars. TOI-4641b is the second such Jovian-sized planet around a rapidly rotating early-type star, preceded only by Kepler-448b (Bourrier et al. 2015; Johnson et al. 2017). Both planets have been found in well-aligned geometries, whereas early-type stars with closer orbiting giant planets tend to show a broad range of obliquities including nearly polar and retrograde orbits.

ACKNOWLEDGEMENTS

DATA AVAILABILITY

The data underlying this article will be shared on reasonable request to the corresponding author.

REFERENCES

Albrecht S. et al., 2012, ApJ, 757, 18
Albrecht S. H., Dawson R. I., Winn J. N., 2022, PASP, 134, 082001
Bate M. R., 2018, MNRAS, 475, 5618
Bate M. R., Lodato G., Pringle J. E., 2010, MNRAS, 401, 1505
Batygin K., 2012, Nature, 491, 418
Borderies N., Goldreich P., Tremaine S., 1984, ApJ, 284, 429
Bourrier V. et al., 2015, A&A, 579, A55
Bourrier V., Cegla H. M., Lovis C., Wyttenbach A., 2017, A&A, 599, A33
Brown T. M. et al., 2013, PASP, 125, 1031
Buchhave L. A. et al., 2010, ApJ, 720, 1118
Buchhave L. A. et al., 2012, Nature, 486, 375
Castelli F., Kurucz R. L., 2004, A&A, 419, 725
Claret A., 2017, A&A, 600, A30
Claret A., Bloemen S., 2011, A&A, 529, A75
Collier Cameron A. et al., 2010, MNRAS, 407, 507
Collins K. A., Kielkopf J. F., Stassun K. G., Hessman F. V., 2017, AJ, 153, 77
Cutri R. M. et al., 2003, 2MASS All Sky Catalog of point sources
Cutri R. M. et al., 2021a, VizieR Online Data Catalog, p. II/328
Dawson R. I., Johnson J. A., 2018, ARA&A, 56, 175
Donati J. F., Semel M., Carter B. D., Rees D. E., Collier Cameron A., 1997, MNRAS, 291, 658
Dotter A., 2016, ApJS, 222, 8
Eastman J., Gaudi B. S., Agol E., 2013, PASP, 125, 83
Fűrész G., 2008, PhD thesis, Univ. Szeged
Fielding D. B., McKee C. F., Socrates A., Cunningham A. J., Klein R. I., 2015, MNRAS, 450, 3306
Foucart F., Lai D., 2011, MNRAS, 412, 2799
Gaia Collaboration, 2023, A&A, 674, A1
Garcia-Mejia J., Charbonneau D., Fabricant D., Irwin J., Fata R., Zajac J. M., Doherty P. E., 2020, in Marshall H. K., Spyromilio J., Usuda T., eds, Proc. SPIE Conf. Ser. Vol. 11445, Ground-based and Airborne Telescopes VIII. SPIE, Bellingham, p. 114457R
Gray R. O., Corbally C. J., 1994, AJ, 107, 742
Guerrero N. M. et al., 2021, ApJS, 254, 39
Heller C. H., 1993, ApJ, 408, 337
Høg E. et al., 2000, A&A, 355, L27
Howell S. B., Everett M. E., Sherry W., Horch E., Ciardi D. R., 2011, AJ, 142, 19
Huang C. X. et al., 2020, Res. Notes Am. Astron. Soc., 4, 204
Irwin J. M., Berta-Thompson Z. K., Charbonneau D., Dittmann J., Falco E. E., Newton E. R., Nutzman P., 2015, in 18th Cambridge Workshop on Cool Stars, Stellar Systems, and the Sun. p. 767, preprint (arXiv:1409.0891)
Jenkins J. M., 2002, ApJ, 575, 493
Jenkins J. M. et al., 2010, in Radziwill N. M., Bridger A., eds, Proc. SPIE Conf. Ser. Vol. 7740, Software and Cyberinfrastructure for Astronomy. SPIE, Bellingham, p. 77400D
Jenkins J. M. et al., 2016, in Chiozzi G., Guzman J. C., eds, Proc. SPIE Conf. Ser. Vol. 9913, Software and Cyberinfrastructure for Astronomy IV. SPIE, Bellingham, p. 99133E
Jenkins J. M., Tenenbaum P., Seader S., Burke C. J., McCauliff S. D., Smith J. C., Twicken J. D., Chandrasekaran H., 2020, in Jenkins J. M., ed., Kepler Data Processing Handbook: Transiting Planet Search, Kepler Science Document KSCI-19081-003, p. 9
Jensen E., 2013, Astrophysics Source Code Library, record ascl:1306.007
Johnson M. C., Cochran W. D., Addison B. C., Tinney C. G., Wright D. J., 2017, AJ, 154, 137
Koposov S., 2020, segasai/minimint: First official release. Zenodo,
Kovács G., Zucker S., Mazeh T., 2002, A&A, 391, 369
Kraft R. P., 1967, ApJ, 150, 551
Kreidberg L., 2015, PASP, 127, 1161
Kuffmeier M., Dullemond C. P., Reissl S., Goicovic F. G., 2021, A&A, 656, A161
Kunimoto M., Tey E., Fong W., Hesse K., Shporer A., Fausnaugh M., Vanderspek R., Ricker G., 2022, Res. Notes Am. Astron. Soc., 6, 236
Kurucz R. L., 1992, in Barbuy B., Renzini A., eds, The Stellar Populations of Galaxies, Vol. 149, Kluwer Academic Publishers Angra dos Reis, Brazil, p. 225
Lai D., 2012, MNRAS, 423, 486
Li J., Tenenbaum P., Twicken J. D., Burke C. J., Jenkins J. M., Quintana E. V., Rowe J. F., Seader S. E., 2019, PASP, 131, 024506
Lightkurve Collaboration, 2018, Astrophysics Source Code Library, record ascl:1812.013
Lin D. N. C., Bodenheimer P., Richardson D. C., 1996, Nature, 380, 606
Lubow S. H., Ogilvie G. I., 2000, ApJ, 538, 326
Mandel K., Agol E., 2002, ApJ, 580, L171
Masuda K., Winn J. N., 2020, AJ, 159, 81
Matsakos T., Königl A., 2017, AJ, 153, 60
McCully C., Daily M., Brandt G. M., Johnson M. C., Bowman M., Harbeck D.-R., 2022, in Ibsen J., Chiozzi G., eds, Proc. SPIE Conf. Ser. Vol. 12189, Software and Cyberinfrastructure for Astronomy VII. SPIE, Bellingham, p. 1218914
McLaughlin D. B., 1924, ApJ, 60, 22
Perryman M. A. C. et al., 1997, A&A, 500, 501

Pont F. et al., 2009, A&A, 502, 695

Queloz D. et al., 2010, A&A, 517, L1

Rasio F. A., Ford E. B., 1996, Science, 274, 954

Ricker G. R. et al., 2015, J. Astron. Telesc. Instrum. Syst., 1, 014003

Rogers T. M., Lin D. N. C., Lau H. H. B., 2012, ApJ, 758, L6

Rossiter R. A., 1924, ApJ, 60, 15

Santerne A. et al., 2014, A&A, 571, A37

Scott N. J., Howell S. B., Horch E. P., Everett M. E., 2018, PASP, 130, 054502

Sikora J., Wade G. A., Rowe J., 2020, MNRAS, 498, 2456

Siverd R. J. et al., 2018, in Evans C. J., Simard L., Takami H., eds, Proc. SPIE Conf. Ser. Vol. 10702, Ground-based and Airborne Instrumentation for Astronomy VII. SPIE, Bellingham, p. 107026C

Skrutskie M. F. et al., 2006, AJ, 131, 1163

Smith J. C. et al., 2012, PASP, 124, 1000

Stassun K. G. et al., 2019, AJ, 158, 138

Stumpe M. C. et al., 2012, PASP, 124, 985

Stumpe M. C., Smith J. C., Catanzarite J. H., Van Cleve J. E., Jenkins J. M., Twicken J. D., Girouard F. R., 2014, PASP, 126, 100

Thies I., Kroupa P., Goodwin S. P., Stamatellos D., Whitworth A. P., 2011, MNRAS, 417, 1817

Twicken J. D. et al., 2018, PASP, 130, 064502

Wijnen T. P. G., Pelupessy F. I., Pols O. R., Portegies Zwart S., 2017, A&A, 604, A88

Winn J. N. et al., 2009, ApJ, 703, 2091

Zhou G., Latham D. W., Bieryla A., Beatty T. G., Buchhave L. A., Esquerdo G. A., Berlind P., Calkins M. L., 2016, MNRAS, 460, 3376

Zhou G. et al., 2019, AJ, 157, 31

This paper has been typeset from a TEX/LATEX file prepared by the author.